TUDelft

Delft University of Technology

Modeling and Analysis of Electric Motors

State-of-the-Art Review

Bilgin, Berker; Liang, Jianbin; Terzic, Mladen V.; Dong, Jianning; Rodriguez, Romina; Trickett, Elizabeth; Emadi, Ali

Citation (APA)

Important note
To cite this publication, please use the final published version (if applicable).
Please check the document version above.

Modeling and Analysis of Electric Motors: State-of-the-Art Review

Berker Bilgin, *Senior Member, IEEE*, Jianbin Liang, Mladen V. Terzic, *Member, IEEE*,
Jianning Dong, *Member, IEEE*, Romina Rodriguez, *Student Member, IEEE*,
Elizabeth Trickett, and Ali Emadi, *Fellow, IEEE*

Abstract—This paper presents a comprehensive state-of-the-art review of the modeling and analysis methods for the multidisciplinary design of electric motors for various applications including vehicular power and propulsion systems and electrified powertrains. It covers the important aspects of different engineering domains, such as dynamic modeling, loss calculations, demagnetization analysis, thermal modeling, acoustic noise and vibration analysis, and mechanical stress modeling. This paper intends to guide the electric motor designers through examples and results on how to apply different analysis techniques on electric motors.

Index Terms—Acoustic noise and vibration, copper losses, core losses, demagnetization analysis, dynamic modeling, electric and hybrid electric vehicles, electric motors, electrified powertrains, mechanical modeling, propulsion systems, spin analysis, thermal modeling.

I. Introduction

ELECTRIC motors designed for traction applications have stringent operational requirements. Traction motors require a wide speed range and high efficiency with high-power density and mechanical robustness. They need to deliver high torque at low speeds and high power at cruising speeds. Due to the extreme loading conditions, traction motors are designed with strict thermal requirements. To satisfy all these requirements, modeling and analysis from multiple engineering domains must be applied when designing an electric motor [1], [2]. Therefore, this paper presents the modeling and analysis methods for the multidisciplinary design of electric motors.

The main purpose of electric motors is to convert electrical input power to mechanical output power. Hence, a dynamic model is needed that represents the relationship between the electrical input and the electromagnetic torque. Various types of motors could be considered for traction applications. Due to

their high power density and high efficiency, permanent magnet synchronous motors (PMSMs) are widely used in traction applications [3]–[5]. Tesla is using a three-phase induction motor (IM) with copper rotor bars in its Model S electric vehicle [1]. The switched reluctance motor (SRM) is a low-cost and robust alternative for traction applications and it does not have coils or permanent magnets (PMs) on the rotor [6]. The dynamic model of an electric motor is dependent on the type of motor and, as it is discussed in Section II, it needs to incorporate the nonlinear flux linkage characteristics.

The electric current and the magnetic flux generate losses in the windings and in the magnetic cores. These are the copper and core losses, respectively, and they are the most dominant loss components that affect the motor efficiency [7]. Section III presents the modeling techniques of core and copper losses in electric motors. This section also addresses the important aspects that affect the loss estimation.

In PM motors, demagnetization analysis is an integral part of the design process to define the performance of a traction motor at a certain operating temperature [8]. The motor geometry and design parameters have to be adjusted to prevent irreversible demagnetization of PMs; otherwise, it would cause a significant reduction in output torque. As detailed in Section IV, demagnetization analysis considers the magnetization characteristics of a PM, motor geometry, operating temperature, and also the negative field from the stator windings.

Traction motors are expected to perform robustly under extreme temperature conditions. Besides, PMs that are commonly used in traction motors are highly sensitive to temperature. Therefore, thermal management is a crucial aspect in electric motor design, but thermal modeling can be a complex issue. Many parameters, such as material properties, heat transfer coefficients, geometry restrictions, and boundary conditions play important roles in developing an accurate model [9]. Section V presents the thermal modeling in electric motors, and provides an example case, which shows how to select the convective heat transfer coefficient when modeling the thermal resistance in the airgap.

Acoustic noise and vibration can be a significant issue in high-torque-density electric traction motors [10]. Numerical methods are generally used for the modeling of acoustic noise and vibration analysis. Section VI presents the important aspects of selecting the element type and element size of the

meshing and contacts for these analyses as they affect the accuracy and computation cost. This section also discusses how to model the relationship among the electrical parameters, motor geometry, airgap forces, and the acoustic noise and vibration.

Finally, to ensure reliable operation, the components of an electric motor drive (EMD) system, such as shafts, bearings, and couplings need to be analyzed from a mechanical perspective. In PM motors, spin analysis needs to be conducted to ensure that the mechanical stress on the bridges at high speeds is lower than the yield strength of the lamination material [9]. Different numerical analysis methods are utilized for the spin analysis, rotor dynamics analysis, static stress analysis, and fatigue analysis, and they are discussed in Section VII.

II. DYNAMIC MODELING AND ANALYSIS

There are many different aspects of dynamics in electric motors. The spatial harmonics brought by slotting, the variation of saturation, and cross-coupling caused by different current pairs, skin effect, switching, and control strategy of power electronics converters will affect the electromagnetic behavior of the systems. The varying losses and cooling conditions at different operating points will change the thermal dynamics of the system. Torque, rotating speed, and electromagnetic forces will affect the mechanical response. Therefore, the dynamics in an EMD should be modeled in a coupled way, or decoupled with reasonable assumptions. This section focuses on the electromagnetic dynamic modeling of electric motors.

A traditional way to describe the electromagnetic dynamics of any electrical motor is using a set of homogeneous linear differential equations including voltage equations, flux linkage equations, and torque equations. Those equations using constant motor parameters are not able to consider the nonlinearity brought either by saturation, skin effect, or spatial harmonics.

Nowadays, the most straightforward way to account for electromagnetic nonlinearity mentioned above is to use the circuit-coupled time-stepping finite element analysis (FEA) [11]. However, once switching or cosimulation with other systems is involved, the numerical method becomes time-consuming. Various measures are proposed to consider nonlinearity in dynamic modeling of different types of motors without repeating transient FEA.

A. Switched Reluctance Motors

The differential equations describing the electromagnetic dynamics of the m-phase SRM are

$$u_i = R_s i_i + \frac{\mathrm{d}\psi_i(i_i, \theta)}{\mathrm{d}t}, \quad i = 1, 2, \cdots, m \quad T_i(\theta, i_i) = \frac{\partial W_i'}{\partial \theta} \tag{1}$$

where u_i is the voltage applied to phase i, R_s is the phase resistance, i_i is the phase current, ψ_i is the phase flux linkage, θ is the rotor electrical angular position, and W_i' is the coenergy.

The SRM requires magnetic nonlinearity to use the coenergy sufficiently so that the torque/mass ratio is maximized. As a consequence, nonlinear modeling is prevailing
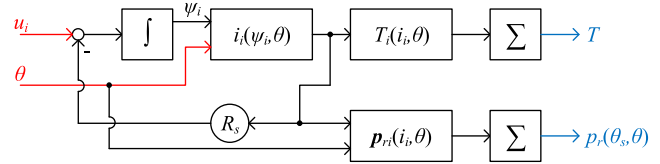

Fig. 1. Dynamic model of SRM based on current-flux linkage LUTs.

in SRM design. Due to the phase-decoupling nature of SRM, phase flux lookup table (LUT) can be obtained from static FEA simulations at different rotor positions with different phase current excitation. Similarly, the torque LUT can also be generated. For ease of numerical integration, the flux linkage LUT is often inverted to obtain the current LUT as a function of flux linkage and rotor position [12], [13]. Fig. 1 shows the dynamic model built based on the LUTs. p_r in Fig. 1 is the radial force distribution as a function of stator position θ_s and rotor position θ, which can be used for modeling of mechanical dynamics, especially vibration and acoustic noise.

The other approach for SRM dynamic modeling is to use incremental inductance models by expanding (1) as

$$\begin{aligned} u_i &= R_s i_i + \frac{\partial \psi_i}{\partial i_i} \frac{\mathrm{d}i_i}{\mathrm{d}t} + \frac{\partial \psi_i}{\partial \theta} \frac{\mathrm{d}\theta}{\mathrm{d}t} \\ &= R_s i_i + l(\theta, i_i) \frac{\mathrm{d}i_i}{\mathrm{d}t} + i\omega \frac{\partial L(i, \theta)}{\partial \theta}, \quad i = 1, 2, \cdots, m \end{aligned} \tag{2}$$

where l and L are the phase incremental inductance and phase self-inductance, respectively and ω is the rotor angular speed. The incremental inductance-based modeling requires at least one additional LUT and has one differentiator involved, which affects the accuracy of the model. Despite the disadvantages, this approach is widely used for control purposes [14].

Apart from modeling based on FEA generated LUTs, there are analytically based and reluctance network-based modeling approaches [15]–[17]. They use analytical expressions or networks to derive ψ_i, as a function of i_i and θ, or vice versa. Those methods are not as accurate as LUT-based modeling. However, they totally or partially eliminate finite element simulations and are suitable for design optimization due to shorter calculation time and ease of parameterization.

B. Synchronous Motors

Synchronous reluctance motor (SynRM) and PMSM are widely used in modern electrical drives because of their high-power density and dynamic performance. Unlike SRMs, phase windings of synchronous motors are coupled with each other. To simplify the model, their electromagnetic dynamics are often described in the $\alpha\beta$ and dq reference system as follows:

$$\boldsymbol{u}_{\alpha\beta} = R_s \boldsymbol{i}_{\alpha\beta} + \frac{\mathrm{d}\boldsymbol{\psi}_{\alpha\beta}}{\mathrm{d}t}; \quad \boldsymbol{\psi}_{dq} = \boldsymbol{\psi}_{\alpha\beta} e^{j\theta}$$

$$T = \frac{3}{2} p(\psi_d i_q - \psi_q i_d) + \frac{\partial W_j'}{\partial \theta} \tag{3}$$

where $\boldsymbol{u}_{\alpha\beta}$, $\boldsymbol{i}_{\alpha\beta}$, and $\psi_{\alpha\beta}$ are the voltage vector, current vector, and flux linkage vector in the $\alpha\beta$ reference frame, respectively; ψ_{dq} is the flux linkage in the dq reference frame, which is determined by i_d and i_q together; and p is the number of pole pairs. W_j' is the magnetic coenergy [18].
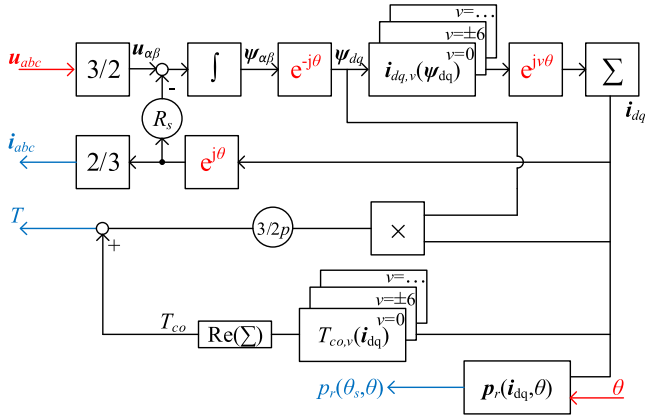
Fig. 2. Dynamic model of the three-phase synchronous motor based on current-flux linkage LUTs.

Fig. 3. Dynamic model of three-phase induction motor.

Fig. 4. Rotor dynamic models considering skin effect.

Nonlinearity in synchronous motors is caused by the rotor position and saturation-dependence of the parameters, as well as cross-coupling between d- and q-axis. Nonlinearity can be modeled using current-flux linkage LUTs as that for SRM. However, the dimension of the LUTs is higher [19]

$$i_{dq} = i_{dq}(\psi_d, \psi_q, \theta). \qquad (4)$$

To improve the accuracy of the interpolation, the rotor dependence of LUT is often considered in spatial harmonics. For a healthy three-phase synchronous motor, the spatial harmonics have the order of multipliers of 6 [13], [18]

$$i_{dq} = \sum_{v=0,\pm6,\pm12...} i_{dq,v}(\psi_{dq}). \qquad (5)$$

A block diagram of the dynamic model based on (5) is shown in Fig. 2.

Apparently, to make the LUTs, FEA has to be repeated on a grid of dq current pairs and rotor positions (usually 60 points per electrical cycle give accurate enough results), then the flux linkage-current LUTs should be inverted, and fast Fourier transformation (FFT) has to be applied to obtain the LUTs in the frequency domain [13]. The procedure needs automatic parametric analysis and can be time-consuming if it is not done properly, because of the high number of repeating FEA calculations. A simplified approach is proposed in [20], which neglects harmonics higher than ±12th and uses only five field solutions. It removes the necessity of FFT and can reduce the computation time by 80%.

Similar to that of SRM, there are also variable inductance based dynamic modeling approaches for synchronous motors. If the cross-coupling effect is considered, the flux linkage equation becomes

$$\begin{aligned}\psi_{dq} &= L_{dq}i_{dq} + \psi_m \\ &= \begin{pmatrix} L_{dd} & L_{dq} \\ L_{qd} & L_{qq} \end{pmatrix}\begin{pmatrix} i_d \\ i_q \end{pmatrix} + \begin{pmatrix} \psi_m \\ 0 \end{pmatrix}\end{aligned} \qquad (6)$$

where ψ_m is the flux linkage from the PM in case of PM synchronous motor (PMSM), L_{dq} and L_{qd} are the mutual inductances in the dq reference frame. Obviously, to consider the cross-coupling, at least one matrix has to be constructed compared to the current-flux linkage approach. To ideally
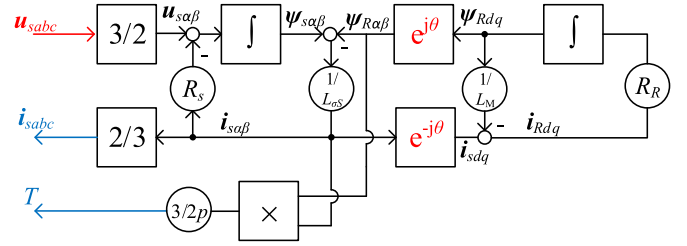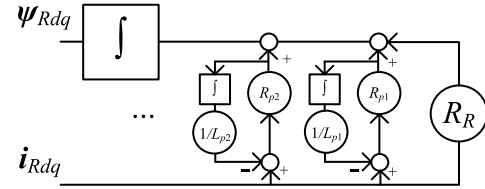
decouple the PM generated flux linkage from the current related components, the saturation level of the magnetic material in each element of the FEA model at each operation point should be frozen, as presented in [21] and [22].

C. Induction Motors

Similar to synchronous motors, dynamics of squirrel-cage IM is often described in the dq reference frame aligned to the rotor flux, assuming all flux linkage is concentrated in the stator [23]

$$u_{s\alpha\beta} = R_s i_{s\alpha\beta} + \frac{d\psi_{s\alpha\beta}}{dt}; \quad \psi_{s\alpha\beta} = \psi_{R\alpha\beta} + L_{\sigma s}i_{s\alpha\beta}$$

$$0 = -R_R i_{Rdq} + \frac{d\psi_{Rdq}}{dt}; \quad \psi_{Rdq} = L_M(i_{sdq} - i_{Rdq})$$

$$\psi_{Rdq} = \psi_{R\alpha\beta}e^{j\theta}; \quad i_{Rdq} = i_{R\alpha\beta}e^{j\theta}$$

$$T = \frac{3}{2}p(\psi_{R\alpha}i_{R\beta} - \psi_{R\beta}i_{R\alpha}) \qquad (7)$$

where subscript s and R represent stator and rotor quantity, respectively; L_M and $L_{\sigma S}$ are the magnetizing inductance and leakage inductance, respectively; θ is the electrical angular position of the rotor flux. Based on the above equations, the dynamic model of three-phase IM is shown in Fig. 3.

The dynamic model of IM is more complicated compared to the other two motors discussed above, because of the additional rotor circuit. Moreover, IM also relies on eddy current to operate, which makes the model parameters both current- and frequency-dependent. To consider the frequency dependence, skin effect in the rotor circuit should be considered. It is often modeled by parallel $L-R$ branches with lumped impedances [23], [24], as shown in Fig. 4.

The lumped parameters can be fitted from measurements or FEA models. To consider the saturation inside IM, an offline current-flux linkage LUT or a function can also be used to replace the inductance (as in the synchronous motor). However, the magnetizing current (i_{sdq}-i_{Rdq}) should be used

as the state variable [25], which makes it more challenging to obtain accurate results from FEA or experiments. Reluctance network-based model can also be used to reduce the calculation effort [26].

III. LOSS MODELING AND ANALYSIS

An important aspect of electrical motor design and analysis is the prediction of the losses for a wide range of speed and load. The most dominant loss components that determine the efficiency of an electric motor are the iron losses in the magnetic core and the copper losses in the stator windings, which are focused in this section.

A. Iron Loss Modeling

Different models have been developed for the iron losses, both from the engineering and physics perspectives. These models generally require compromise among the details of loss characteristics of the magnetic material, accuracy, simplicity, and computation time. All these methods can be divided into three groups, according to the calculation approach [27], [28]. The first group, which is also historically the oldest approach, is based on the Steinmetz equation

$$p_{Fe} = C_{SE} f^{\alpha} B_m^{\beta} \qquad (8)$$

where B_m is the peak value, f is the frequency of the flux density in the lamination sheet, and C_{SE}, α, and β are the core loss coefficients determined by fitting the loss model to the measurement data. Even though Steinmetz based models are easy to implement and require a small amount of information on the magnetic material properties, their accuracy is low.

The second group of methods considers the separation of iron loss based on frequency, alternating and/or rotating flux density, and harmonic analysis. The first model of this group is an extension of (8), where the iron losses are separated into static hysteresis losses p_{hyst}, and dynamic eddy current losses p_{ec} [28]:

$$p_{Fe} = p_h + p_e = C_h f B_m^n + C_e f^2 B_m^2 \qquad (9)$$

where C_h and C_e are hysteresis and eddy current loss coefficients, and n is the hysteresis loss exponent, which has a typical value of two. For higher accuracy, it is calculated as a function of the peak flux density [29]. Excess loss component was added to (9), which is modeled as [30]

$$p_{ex} = C_{ex} f^{1.5} B_m^{1.5}. \qquad (10)$$

Equations (9) and (10) are usually referred to as the Bertotti formula. The physical description and function of the excess loss factor C_{ex} can be found in [31]. The expressions in (9) and (10) are usually exploited by commercial FEA software packages due to the ease of implementation and moderate accuracy. For a nonsinusoidal magnetic field, these expressions can be applied to each harmonic component separately and then the total loss is obtained by superposition of separate harmonic contributions. The time-domain expression of (9) and (10) is used directly in time stepping FEA, while the
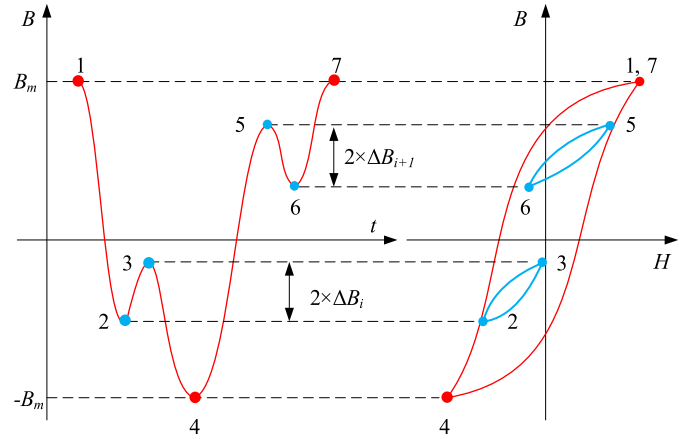

Fig. 5. Minor hysteresis loops due to the local extremums in the magnetic induction waveforms.

frequency domain expression is applied in the FEA postprocessing calculations after the magnetic flux harmonics components are obtained [27].

Another approach to consider the nonsinusoidal field is to modify the hysteresis term in (9) to take into account the minor hysteresis loops that appear due to the local extremums in the magnetic induction waveform (see Fig. 5) while keeping the excess loss term as in (10). This model in the time-domain can be expressed as [32]

$$p_{Fe} = \frac{C_e}{\pi^2} \frac{\gamma}{T} \int_0^T \int_{\text{iron}} \left(\frac{dB}{dt} \right)^2 dv dt + \frac{C_h \gamma}{T} \int_{\text{iron}} B_m^{\alpha}$$
$$\times \left(1 + \sum_{i=1}^{l} \frac{\beta}{B_m} (\Delta B_i) \right) dv$$
$$+ \frac{C_{ex} \gamma}{T} \int_0^T \int_{\text{iron}} \left| \frac{dB}{dt} \right|^{1.5} dv dt \qquad (11)$$

where T is the period, B and B_m are the instantaneous and maximum flux densities in the considered period, ΔB_i is the local amplitude of the flux density that causes minor hysteresis loss, and l is the number of the minor hysteresis loops. This approach, with slight modifications, is successfully applied in a SRM, which exhibits extremely nonsinusoidal magnetic field variation [33]. A modified version of (9) and (10) with variable coefficients can also be used to account for additional losses in pulsewidth modulation (PWM) inverter fed motors [34]. In [35], the authors have proposed a modification to (11) with variable coefficients (induction, frequency, and temperature dependence) for the calculation of iron losses in PWM inverter fed motor drives. The proposed modification provides important modeling capabilities, since PWM switching causes many minor hysteresis loops.

Finally, iron loss models in the third group are based on the mathematical representation of the hysteresis loops [28], [36]. These models can be used if the complete hysteresis loop is obtained from the measurements, which makes these models unpractical and more complex for implementation. Therefore, they are seldom used in electric motor design, even though they tend to provide high accuracy in iron loss calculation.

B. Effect of Manufacturing on Iron Loss Estimation

The prediction of the iron loss strongly depends on the manufacturing process, namely lamination cutting/punching, stacking, and welding. The effect of these manufacturing processes on each of the iron loss components, as well as on the saturation magnetization and the coercive field strength are summarized in [37].

The lamination cutting procedures generate additional loss due to the decrease in magnetic permeability and, hence, increase in loss density. Several modified iron loss models have been developed to account for these additional losses. The first approach, which is still widely used in the industry, is to include a region of uniformly degraded material along the edge of the lamination [38], [39]. The $B-H$ curve of the degraded material region is usually determined by fitting the iron loss measurement results to the calculated values to obtain the smallest deviation.

The second approach is to introduce the continuous function of cut-edge distance for presenting the magnetic degradation [40], [41]. This model suffers from the difficulty of reproducing the measurement results from a proposed loss model due to a nonlinear relationship of cut-edge distance with the permeability and core-loss density. Besides, the solution of this model in FEA is time-consuming. To solve these issues, a new model is presented in [42], which includes the cut-edge effect in the hysteresis coefficient.

It is worth noting that despite the variety of models, there is no strictly defined (standardized) procedure in literature for the core loss estimation. Electric motor designers still have to rely on their engineering expertise and knowledge to select the proper model in each specific design case.

C. Copper Loss Modeling

Losses in the windings are traditionally divided into two main components: dc and ac losses. AC losses are caused by skin-effect, proximity effect, circulating currents (uneven distribution of the total current between parallel strands caused by the field of nearby conductors), and slot effect (tendency of the current to localize in the conductors, which are near the slot opening, caused by the leakage flux of all conductors in the slot). Besides, PWM switching frequency can also affect the proximity component of ac copper losses. This has been verified mostly by measurements and FEA in [43] and [44], respectively. There are basically three main approaches for the modeling of copper losses: analytical method, FEA, and hybrid method, which combines the first two methods.

For form-wound winding (rectangular conductors placed regularly into the slot), the computation of ac losses can be modeled analytically by calculating the resistance factor

$$K_R = \frac{R_{ac}}{R_{dc}} = \frac{P_{ac}}{P_{dc}} \tag{12}$$

where R_{ac} and R_{dc} are the resistances, and P_{ac} and P_{dc} are losses due to ac and dc currents, respectively. The way to calculate K_R is to first determine the current density distribution J in the conductors, which can be expressed as a function of reduced conductor height, ξ. For a single conductor

in the slot, it is defined as [45]

$$\xi = h_c \sqrt{\frac{1}{2} \omega \mu_0 \sigma_c \frac{b_c}{b}} \tag{13}$$

where h_c is the conductor height, ω is the angular frequency of the current, μ_0 is the permeability of vacuum, σ_c is conductivity of the conductor, and b_c and b are width of the conductor and the slot, respectively. The current distribution is then used to calculate P_{ac}, which is then applied in (12) to calculate K_r as a function of ξ. There are many equations which define ξ as a function of conductor distribution and connections in the slot [46]–[48]. Circuit method can also be used for analytical calculation of ac winding losses [45]. There are also other methods developed for different winding types [49]–[51]. However, they often require some assumptions and simplifications, which might limit their applicability to some specific cases [52].

For more complicated winding arrangements and slot geometries, FEA-based numerical computation is usually employed, which can offer general applicability and higher accuracy. However, the FEA approach requires more computational resources and time, especially if the exact winding is modeled with all conductors and separate strands. This increases the number of mesh elements and, hence, the computational time. One widely used FEA approach is squared-field derivative method (SFD). It is based on the postprocessing of the field results and it assumes that magnetic induction is homogenous in the cross section area of the wire. This method does not require deep access to FEA solver and it can usually offer good enough accuracy, which might be critical when skin depth is small and there are large circulating currents [53].

Recent improvements in the SFD method have been introduced where slot leakage field is obtained through magnetostatic simulations (coils are modeled as bulk conductive regions with homogenous current density) and then are applied as an external field in the analytical model [54]. The external field is combined with the field produced by other nearby conductors to calculate the current distribution in each strand. The model has been shown to provide good accuracy and high computational speed.

Another FEA-based method is the homogenization principle [55]. The fine winding structure is modeled as a region with complex reluctivity where the imaginary part represents the losses. Hence, ac copper losses are calculated similar to iron losses by integrating the surface of the $B-H$ curve. This method is a postprocessing calculation and it can be applied either in frequency or time-domain.

In order to overcome the long computation time and high computation power for FEA analysis, macroelement approach has been applied where the slots of the motor are modeled by their impulse response functions. This method considers all loss components with the same accuracy as the standard FEA, but with speedups of 70–100 times [56].

IV. DEMAGNETIZATION ANALYSIS

Demagnetization analysis is an important and necessary process in PM motor design. Irreversible demagnetization of
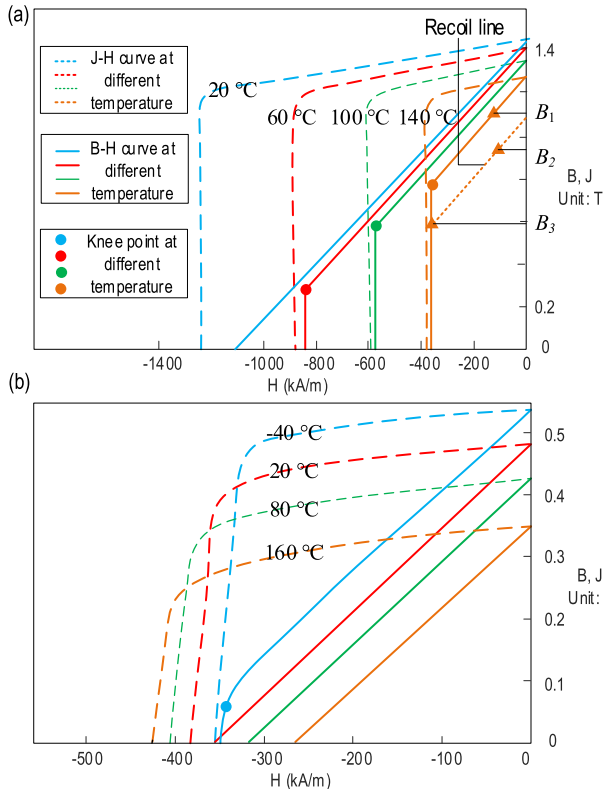
Fig. 6. Demagnetization characteristics of permanent magnet. (a) Rare earth magnet [58]. (b) Ferrite magnet [59].
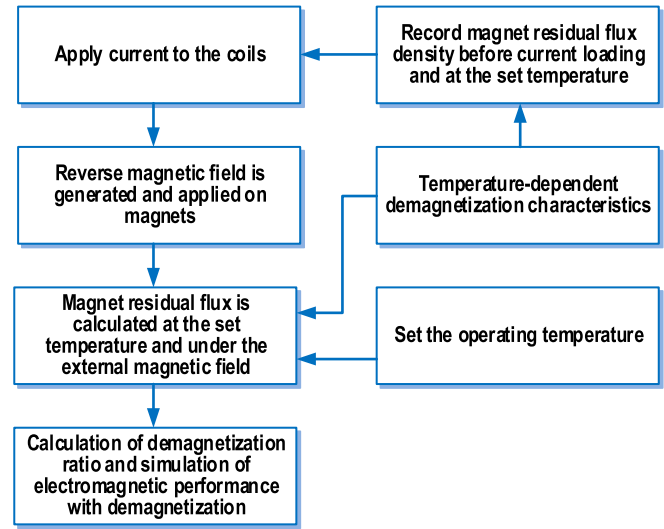

Fig. 7. Flowchart of demagnetization analysis [61].

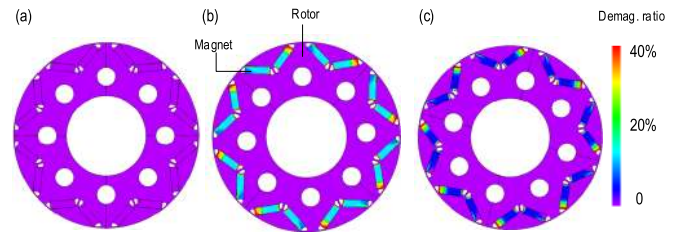
Fig. 8. Magnet demagnetization ratio in an IPM motor. (a) Temperature set to 80 °C. (b) Temperature set to 150 °C. (c) Back to 80 °C.

the PMs can cause a significant decrease in output torque and, hence, reduced reliability. High operating temperature is one of the factors that can lead to demagnetization of rare earth magnets.

As shown in Fig. 6(a), the magnetic field strength at the knee-point in rare earth magnets decreases dramatically at elevated temperature. If the reverse field applied during the motor operation is high enough so that the magnet operates below the knee point, the magnet would be irreversibly demagnetized. Electric motors with ferrite magnets are also vulnerable to irreversible demagnetization due to the low coercive force of the ferrite magnets [57]. The demagnetization characteristics of ferrite magnets are different from that of rare earth magnets. As shown in Fig. 6(b), the magnetic field strength at the knee points of ferrite magnets become smaller at lower temperatures. Therefore, the demagnetization analysis for ferrite magnets should be conducted at low temperatures.

Demagnetization can be simulated in FEA. Fig. 7 shows the flowchart of the demagnetization analysis of PMs in electric motors. After applying current to the coils, the reverse magnetic field is generated and applied on the magnets. The magnet residual flux can be simulated based on the temperature-dependent demagnetization characteristics of the magnets. Then, the demagnetization ratio can be calculated as shown in the following equation [60]:

$$\text{Demagnetization ratio}(\%) = 100 \times \left(1 - \frac{B_2}{B_1}\right). \quad (14)$$

In (14), B_1 is the magnet residual flux density before current loading and B_2 is the magnet residual flux density after the loading at the set temperature. Fig. 6 shows an example of the demagnetization analysis. Before the current loading at the set temperature, the operating point of the magnet is at B_1. When the current loading is applied, the operating point of the magnet passes the knee point at B_3. When the current loading is removed, the operating point of the magnet moves along the recoil line to B_2.

Fig. 8 shows the demagnetization analysis of an interior permanent magnet motor (IPM) with rare earth magnets. Different thermal conditions are applied to the IPM in three different stages. First, the temperature of the magnet is set at 80 °C and the demagnetization ratio of the magnet is shown in Fig. 8(a). Then, the temperature of the magnet is increased to 150 °C. Demagnetization can be observed in a large area of the magnet shown in Fig. 8(b). Finally, the temperature of the magnet reduced back to 80 °C. Compared with Fig. 8(a) at the same temperature, demagnetization still appears at the magnets shown in Fig. 8(c). This is because irreversible demagnetization occurred when the temperature was increased to 150 °C.

The effect of irreversible demagnetization on average torque can also be observed in the torque waveform of the motor, as shown in Fig. 9. Due to irreversible demagnetization, the average torque in stage 3 cannot recover when the temperature of the magnet decreases from 150 °C to 80 °C.
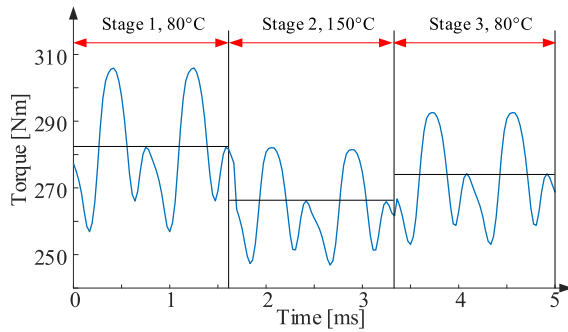
Fig. 9. Decrease of average torque caused by irreversible demagnetization of magnets at high temperature.

Fig. 10. Electric motor design methodology using thermal analysis.

V. THERMAL MODELING AND ANALYSIS

A. Overview of Thermal Modeling

Thermal management is a crucial aspect of electric motor design. With thermal modeling, the goal is to calculate the temperature distribution of a motor to evaluate whether the thermal management strategy is sufficient in maintaining components below their critical temperatures, such as coil temperature. Developing an accurate thermal model requires accurate simulation of the losses as well as the thermal management strategy. Determining the heat transfer coefficients, material properties, geometry simplifications, and boundary conditions are vital in thermal modeling, and valid heat transfer assumptions must be made in the thermal analysis [62].

Various thermal management techniques exist for electric machines depending on their cooling needs [63]. Common cooling strategies include air-cooling (external and internal fans [64], [65]), liquid-cooling (direct cooling of windings or cooling jacket [66], [67]), oil-cooled systems [68], or some combination of these methods [69]. Modeling each of these complex cooling systems along with the motor geometry and losses requires employing FEA and computational fluid dynamics (CFD) tools. Typically, a combination of FEA, CFD, and lumped parameter thermal network (LPTN) are used to develop high fidelity models of electric machines.

Thermal response of an electric motor may be described by using the thermal circuit analogy, where the temperature difference (ΔT) is analogous to voltage, heat transfer rate, q is analogous to current, and thermal resistance (R_{thermal}) is analogous to electrical resistance. Hence, the steady-state equation for the heat transfer rate [W] is

$$q = \frac{\Delta T}{R_{\text{thermal}}} \tag{15}$$

For a lumped system, the thermal time constant τ_{thermal} is defined by the component's thermal capacitance, $\rho c V$, and the thermal resistance as

$$\tau_{\text{thermal}} = R_{\text{thermal}} C_{\text{thermal}} = \frac{1}{hA} \rho c V \tag{16}$$

For transient simulations, the temperature can rise quickly if the component's thermal energy storage is small: i.e., low-density ρ, low specific heat c, small volume V, large convective heat transfer coefficient h or large surface area A. When an RC thermal network is used to describe a complex system
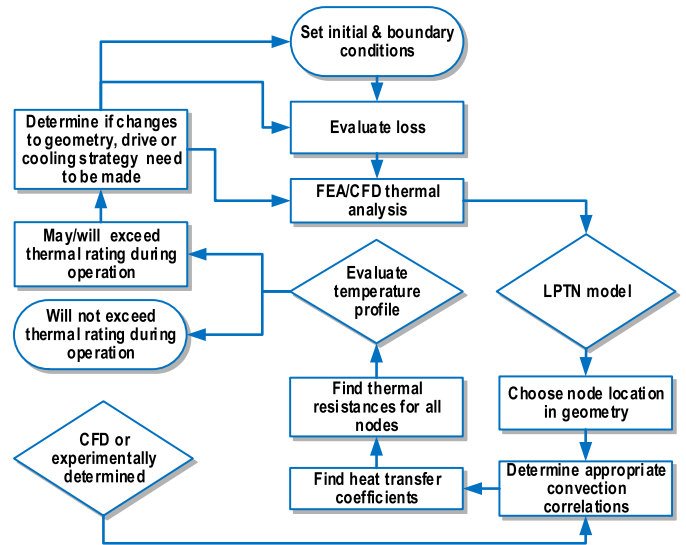
like a motor, it is often described as an LPTN. The nodes of an LPTN simplify the spatial temperature distribution of the real geometry and several components are lumped into single node The accuracy of LPTN models relies on the node placement, number of nodes, and the calculated values of $R_{\text{thermal}} C_{\text{thermal}}$ for each node [70].

CFD is useful for modeling convective heat transfer in complex fluid flow, such as the airflow around end-windings and FEA, is useful for modeling heat conduction in non-standard rotor/stator geometry. While FEA/CFD can be more accurate, they also rely on correct input parameters to deliver accurate results. For example, the contact resistance between the winding and insulation needs to be modeled with an effective thermal conductivity to capture an accurate temperature distribution [71]. Also, setting up a mesh with good quality for a motor geometry requires expertise and solving FEA/CFD models is computationally expensive compared to LPTN models [72]. Therefore, LPTN models can be developed by extracting results from FEA/CFD (e.g., effective thermal resistance of the cooling jacket) to perform computationally expensive simulations, such as drive cycle analysis, where the losses are changing temporally and spatially [73]. For further illustration, Fig. 10 shows a simple methodology of the thermal analysis for electric motor design.

Although LPTN models are computationally faster than numerical models, much effort must be invested in obtaining accurate RC values [74]. Determining these thermal resistances is typically difficult since convective thermal resistances have complex dependencies on many different factors such as motor topology, manufacturing conditions (i.e., contact resistance between parts), speed, and temperature. A good starting point is to derive convective heat transfer coefficients from either numerical or experimental correlations found in the literature. Therefore, Section V-B provides a steady-state thermal modeling example to obtain the convective heat transfer coefficient across the mechanical air gap of a motor using correlations. Steady-state for motor thermal model means that
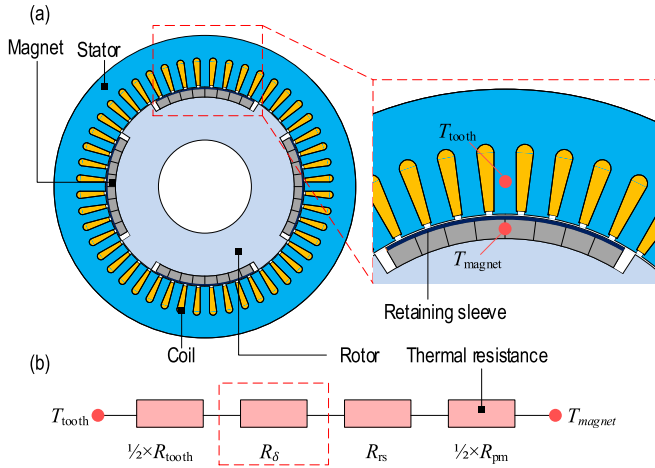
Fig. 11. (a) Nodal placement on the motor. (b) Part of the thermal resistances in the motor, R_δ is the convective thermal resistance being calculated.

Symbol	Parameter	Example
	shape of rotor	cylinder or salient rotor, as well as the shape of the enclosure [77]
g	air-gap width	radially or axially [83], [77], gaps between stator core and housing were investigated in [71]
ω	rotational speed	radians/s when heat transfer is measured per second [77], [84]
Re	flow	of ventilating air or coolant if rotor is enclosed, expressed as the axial flow Reynolds number [71], [78]
L/g	configuration	relative length of the flow path of the ventilating air [85]
Gr	free convection	only during stall or very low speed conditions, expressed using the Grashof number [82]
	surface roughness	most convection correlations relate smooth surfaces however this can be considered a minimum for rough surfaces

the motor has remained at an operating point long enough for all changing parameters and temperatures to stabilize.

B. Example Case–Steady-State Airgap Thermal Modeling

The motor shown in Fig. 11, an inset-magnet PMSM, four-pole rotor totally enclosed motor, will be used as an example. In order to determine the temperature distribution of the motor, one parameter that must be retrieved is the convective heat transfer coefficient.

Heat transfer between the motor and its environment takes place through three physical processes or modes: conduction, convection (forced or natural), and radiation. Within the motor, understanding the temperature of a component requires the evaluation on how these modes are participating in heat transfer between that component and its immediate environment. For instance, a coil may be in conductive contact with a slot liner, which is, in turn, in contact with the stator tooth. With the spinning of the rotor, the coil would also experience some form of forced convection. Radial heat transfer due to convection in the airgap is considered here as an example. Thermal conduction and radiation are briefly addressed at the end of this section.

The nodes shown in Fig. 11 represent part of the thermal network for the motor; the complete thermal model may be seen in [75]. T_{magnet} and T_{tooth} are only two nodes of the many used to represent the motor in the LPTN model. Nodal placement was made based on estimated hot spots from prior experience. As shown in Fig. 11, T_{magnet} is placed at the center of the PMs and represents the temperature of all the magnets in the motor (they are all "lumped" into a single node). T_{tooth} is placed at the center of the stator tooth and there are four thermal resistances between the nodes shown above. R_{tooth} is the thermal resistance of all the stator teeth, R_δ is the convective thermal resistance of the air gap, R_{rs} is the retaining sleeve thermal resistance, and R_{pm} is the thermal resistance of the PMs. The following paragraphs have described how to solve for R_δ, while the other thermal resistances of the model are further described in [58].

Calculating the convective heat transfer through the airgap of an electric motor or any other form of thermal management

strategy, such as spray cooling, can be a cumbersome process since it is dependent on complex fluid flow through the motor. For a given electric motor, its unique geometry of the rotor and stator can cause airflow that is far from the laminar flow. Determining the temperature and velocity profiles of the fluid requires solving the Navier–Stokes and energy equations, which do not have analytical solutions for most complex geometries. Therefore, either numerical methods are used, such as CFD modeling [76], to solve for the convective heat transfer or experiments may be carried out [77]. From these numerical simulations or experimental measurements, correlations are derived representing certain geometries and flow conditions. These correlations, typically presented in the form of nondimensional numbers, may be applied to model other motors with similar geometries and flow patterns.

Many researchers have experimentally investigated the heat transfer and flow phenomena in Taylor–Couette flow (fluid confined between two concentric rotating cylinders) and more recently Taylor–Couette–Poiseuille flow (includes axial flow between rotating cylinders) [78]. If a motor is totally enclosed, Taylor–Couette flow correlations may be used and if a motor is open and axially-cooled, then Taylor–Couette–Poiseuille may be employed [79]–[81] to model the heat transfer in the air gap. Deciding whether an experimental correlation applies to a certain motor is determined by comparing certain factors such as motor geometry and tested speed range. Many factors can impact the heat transfer across the airgap by influencing the fluid flow experienced, as shown in Table I.

The heat transfer correlations are reported by the Nusselt number, Nu, which is a nondimensional number defined as

$$\text{Nu} = \frac{hD}{k} \tag{17}$$

where k is the thermal conductivity of the fluid and h is the heat transfer coefficient, which is the parameter being solved in this example. D is the characteristic length and it is usually determined based on the correlation definition.

Particular attention needs to be paid on how the Nusselt number is defined. For example, D may be defined as D_h (hydraulic diameter) of the airgap or 2δ (twice the airgap length, δ) in a certain correlation. The Nusselt correlations are usually presented as a function of Taylor number, Ta, and Reynolds number, Re. The Taylor number is used as a relative measure of fluid momentum to viscosity between rotating cylinders [62]. The Reynolds number determines the transition between laminar and turbulent flow in axial flow and captures the rotor speed and motor size.

At the given motor speed, the Taylor number and Reynolds number (axial flow condition) must be calculated to assess if the selected experimental correlation is valid. If the Taylor number and Reynolds number are in the same ranges reported in the setup of the experimental correlation, then the correlation can be used.

Since the motor configuration shown in Fig. 11 is enclosed, Taylor–Couette heat transfer correlations may be investigated. The heat transfer correlations from [86] will be used to solve for the thermal resistance R_δ, shown in Fig. 11, for a motor speed of 6000 RPM. The thermal model created in [75], which is used as an example here, was experimentally validated. The rotor has a diameter of 107.1 mm and the mechanical gap is 0.3 mm. The Taylor number is defined as [86]

$$Ta = \frac{\omega^2 r_m \delta^3}{v^2} \tag{18}$$

where ω is the rotational speed in rad/s, v is the kinematic viscosity of the fluid (in this case, air), and r_m is the mean radius of the annulus. Evaluating the Taylor number for an air temperature of 50 °C, the kinematic viscosity is 1.785×10^{-5} m/s and, thus, substituting all the values into (18), it results in 1.7905×10^3 for Ta. It should be noted that the thermal network should be solved to estimate the temperature of all the nodes, and then temperature-dependent properties such as v should be updated. This process is repeated until the solution stops changing, thus the solution procedure is iterative.

The correlations given in [86] are a function of Taylor number and a geometrical factor, F_g. From the experiments conducted in [86], two correlations are reported as a function of the modified Taylor number, which is defined as $Ta_m = Ta/F_g$ for the flow in the air gap that is laminar with vortexes

$$\begin{cases} \text{Nu} = 0.128\left(\dfrac{Ta}{F_g}\right)^{.367}, & 1700 < \dfrac{Ta}{F_g} < 10000, \\[2mm] \text{Nu} = .409\left(\dfrac{Ta}{F_g}\right)^{.241}, & 10000 < \dfrac{Ta}{F_g} < 10^7. \end{cases} \tag{19}$$

Calculating F_g, and plugging this into Ta/F_g evaluates to 1.782×10^3, thus the value falls in the range of the first correlation of (19). Now, the convective heat transfer coefficient may be solved for by rearranging (17) as

$$h = \frac{\text{Nu}k}{2\delta} = \frac{.128\left(\dfrac{Ta}{F_g}\right)^{.367} k}{2\delta} \tag{20}$$

and the thermal resistance, R_δ, shown in Fig. 11, is determined in cylindrical coordinates as

$$R_\delta = \frac{1}{h2\pi r L} \tag{21}$$

where L is the axial length of the rotor and r is the rotor radius. The correlations presented here are valid for a totally enclosed motor, but correlations which are valid for open axially cooled motors are found in [77].

C. Other Thermal Resistance Values

For conduction, components might not be in good contact with each other, creating an effective thermal resistance at an interface, referred to as contact resistance. While it is difficult to know the exact interfacial conditions between the two components, smooth surfaces and pressure applied to the components tend to reduce the contact resistance. When creating an LPTN, the interface can be approximately represented as a circuit in which the two components are at their ideal thermal conductivity (k-values), and their thermal resistances are connected in parallel circuits [87], [88]. In [89], the challenges in determining the contact resistance between the windings and laminations due to manufacturing differences have been investigated and it was highlighted that these parameters must be extracted experimentally.

Radiation can be a concern at high temperatures through gaps for example, between the end windings and end plate, the mechanical air gap or off-the-motor housing. Only component faces, which have a view of one another, participate in heat transfer. Unfortunately, motor components have many faces. Several methods exist to solve these systems: FEA suites have multi-surface solvers that calculate the number of surfaces from CAD models, as well as analytical methods like the radiation network method (note: this is different than an LPTN) and the direct or matrix method [90].

VI. Modeling and Analysis of Vibration and Acoustic Noise

Both analytical and numerical methods can be used to analyze the vibration behavior and acoustic noise in electric machines. The analytical method can provide a faster and more computationally-efficient way. The numerical method is usually more precise because the structural details can be considered in the modeling [91]. Before presenting the details of acoustic noise modeling and analysis, some important modeling aspects, such as the meshing and the contacts between parts for the numerical method, will be discussed.

A. Element Size and Element Type

When using numerical methods for the modeling of acoustic noise and vibration analysis, the element type and element size are important for accuracy and computation cost. For example, compared with a hexahedron element, tetrahedron element is easier to fit and mesh complex geometries. Mesh quality is also easier to achieve with tetrahedron element. Besides, hexahedron can also be problematic when meshing the transitions from the small element size used for a complicated part to
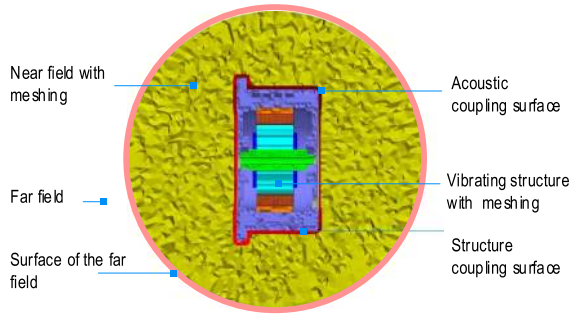
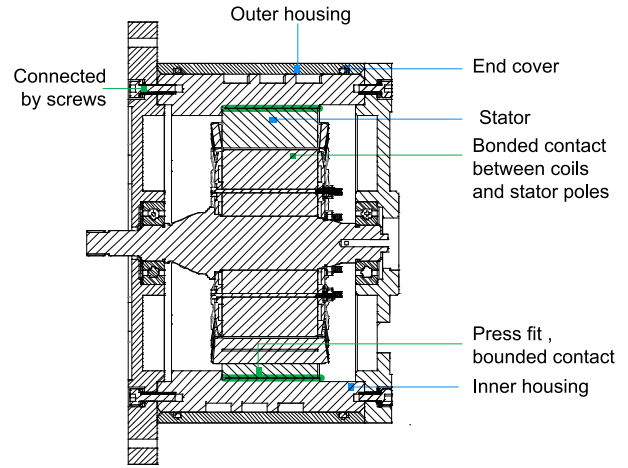Fig. 12.   Meshing for the acoustic noise and vibration analysis.

Fig. 13.   Typical contacts between parts in an electric motor for the numerical acoustic noise and vibration analysis [91].

Fig. 14.   Typical procedures for acoustic noise and vibration modeling.

the larger element elsewhere in the geometry [92]. However, hexahedron is more economic in computation cost compared to the tetrahedron.

In acoustic noise and vibration modeling of an electric motor, the analysis of the noise radiation and emission takes place in three stages: excitation of the stator-frame structure through electromagnetic forces, structure-borne noise transmission, and acoustic noise emission [93]. The simulation of acoustic noise in these stages depends on the meshing of the structure, the near field, and the far-field (see Fig. 12). The near field is where the nature of the sound wave depends on the vibration of the structure. The far-field is where the nature of the sound wave depends on the propagation medium (e.g., air). Tetrahedron element is generally preferred for the meshing of electric motors if the geometry is complex [92]. On the other hand, sensitivity analysis needs to be conducted to make sure that the element size in the meshing of the structure, near field, and far-field are small and fine enough. The near field is often modeled as the internal space of a sphere. In order to ensure the accuracy of the simulation at the expense of a low computation cost, the sphere for the near field should be at least one wavelength thick, which is measured from the surface of the housing.

B. Contacts Between Parts

In the numerical modeling of acoustic noise and vibration, the contacts between different parts affect the stiffness of the vibrating structure and, thus the natural frequencies. When the stator and the inner housing of a traction motor are connected by a press fit, as shown in Fig. 13, the contact between the stator and the inner housing can be modeled as a bonded contact, for a small amplitude of vibration. The contact between the inner housing and the outer housing can also be defined as a bonded contact since the two housings are welded together. However, it is not recommended to model the entire interface between the end cover and the inner housing as a bonded contact. Since the end cover and the inner housing are connected by screws, only the screw region in the interface should be defined as a bonded contact [94]–[96].

C. Modeling of Vibration and Acoustic Noise

The acoustic noise radiated from electric motors can be divided into several categories: electromagnetic noise, mechanical noise, aerodynamic noise, and combined electrical
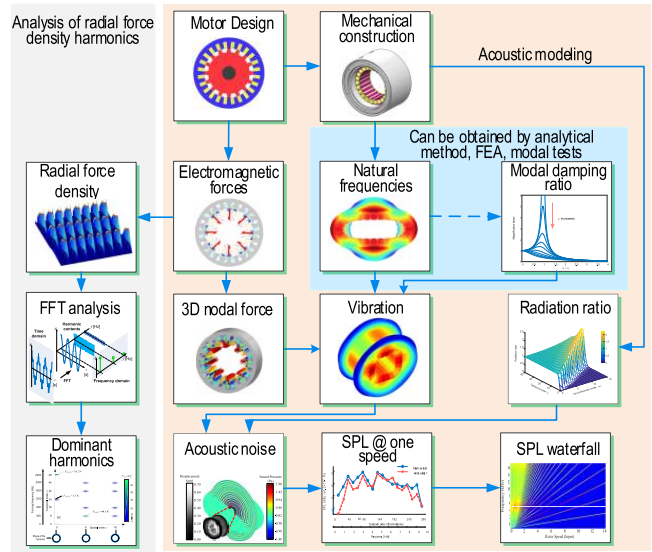
and mechanical noise [13], [93]. Electromagnetic noise significantly contributes to the total acoustic noise of an electric motor. Therefore, this section focuses on the modeling for the prediction of the electromagnetic noise by using either analytical or numerical method. The flowchart in Fig. 14 shows the modeling process for the prediction of acoustic noise. In the analytical method for the acoustic simulation, the radial force density needs to be extracted from the 2-D electromagnetic FEA or generated by the dynamic motor model. In the numerical method, 3-D nodal forces need to be generated. 3-D nodal forces are usually produced by extending the 2-D electromagnetic nodal forces along the axial direction of the motor. This is based on the assumption that the distribution of nodal forces along the axial direction is uniform [97], [98]. FFT can be applied to the 2-D electromagnetic force density to get the dominant harmonic components. Analyzing the dominant harmonics of the radial force density is important for acoustic noise analysis and noise reduction. It helps to develop a deep understanding of the dominant

Fig. 15. Contacts between rotor laminations in the spin analysis. (a) Stacked rotor laminations. (b) Single rotor lamination.
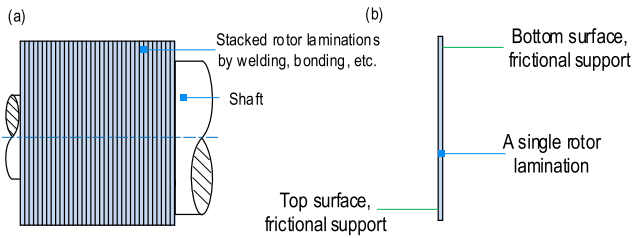
harmonics and the dominant vibration modes in an electric motor.

The natural frequency and the modal damping ratio for each vibration mode can be obtained through analytical methods [99], FEA [100], and modal tests [101], including hammer impulse test and shaker test. Taking the 3-D nodal force, mode shapes, and the modal damping ratio, the vibration behavior and the acoustics of electric motors can be simulated in commercial FEA software. In the analytical method, the vibration, which is simulated by taking the radial force density, natural frequency, and modal damping ratio as inputs, need to be converted into acoustic noise by taking the radiation ratio into account [102]. The radiation ratio is defined as the radiated sound power divided by the surface vibrations of electric motors. The simulation of vibration and acoustics at one speed point can be in the time domain or frequency domain. Repeating the process from the generation of electromagnetic force to the simulation of acoustics, the sound power level (SPL) waterfall diagram in motor's operating speed range can be generated.

VII. Mechanical Stress Modeling and Analysis

Besides the core electromagnetic analysis, electrical motors have to be analyzed regarding the mechanical properties of their rotating components. Some mechanical parameters of the rotor also determine the electromagnetic properties of the motor (e.g., small ribs in IPM, which hold the magnets in place). Therefore, mechanical analysis usually has to be conducted in parallel with electromagnetic analysis. Most common mechanical analysis include spin, static stress, dynamic stress, and rotor-dynamic analysis [103].

A. Spin Analysis

The spin analysis is performed to check the magnitude and the distribution of centrifugal forces in the rotor, its effect on the stress in different rotor parts, and the mechanical integrity of the complete rotor structure at the maximum rotational speed. Analytical methods can be used to calculate the centrifugal stress for some simple structures. For more complicated structures, FEA is preferred to analyze the stress and elongation with higher accuracy. The focus in this section is to present the details of spin analysis for an IPM machine using FEA.

Spin analysis conducted in 3-D usually provides better accuracy as compared to 2-D spin analysis. In an electric motor, rotor laminations are stacked to construct the rotor core, as shown in Fig. 15(a). The rotor laminations can be
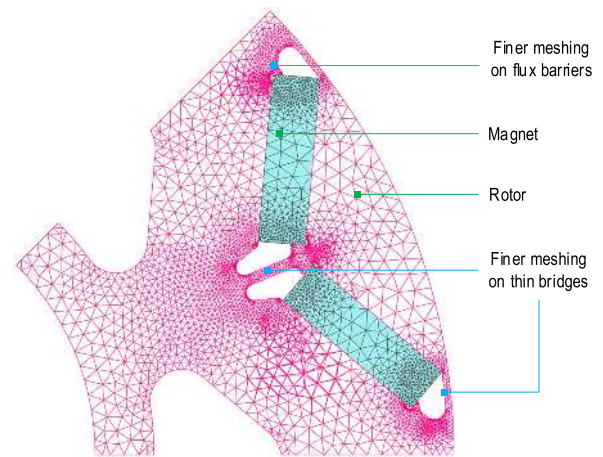

Fig. 16. Meshing of the rotor for the spin analysis.

welded or bonded together. However, to simulate the worst case in terms of mechanical stress, a single piece of lamination should be taken for the 3-D spin analysis [77]. This is because the mechanical stress in a single lamination model is much higher than that in a complete rotor core model when the core is modeled as an entire piece of steel. In some cases, the axial support to a single lamination from the other laminations might not be strong enough due to manufacturing error (e.g., some laminations can be partially separated from the core). Therefore, it is the worst case to consider a single piece of lamination in the spin analysis. As shown in Fig. 15(b), the contact between laminations can be modeled by applying frictionless support on the top surface and the bottom surface of the lamination. It should be noted that the element size of the meshing should be smaller than the thickness of the laminations.

When using numerical methods for spin analysis, the element type and element size are important for accuracy and computation cost. Hexahedron elements can be used for the mesh when the motor has simple rotor and magnet geometries. In high-stress regions, the element size should be small while the larger element size can be applied to the other regions. Fig. 16 shows an example where the rotor and the magnets are meshed for spin analysis. The finer mesh is generated on the thin bridge and the flux barriers on the rotor because high stress is expected to appear in these regions [103]–[105].

The contacts between parts in the 3-D FEA spin analysis are also important for the accuracy of the simulation. The modeling of the contacts should be as close to the actual nonlinear behavior of the contacts in the structure. The type of contact affects how the nodes are connected at the interface of different parts. As shown in Fig. 17, the contact between the epoxy and the rotor lamination, and the contact between the epoxy and magnets should be modeled as a bonded contact. This is because epoxy is used for bonding the parts. On the other hand, the contacts between the rotor core and the magnets should be modeled as a frictional contact. The friction coefficient can be specified based on the material properties of the magnet and the rotor lamination. To reduce the computation cost and increase the accuracy of the simulation, a one-pole model
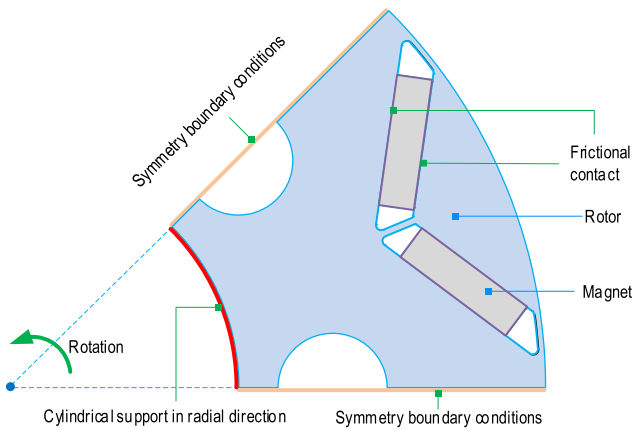
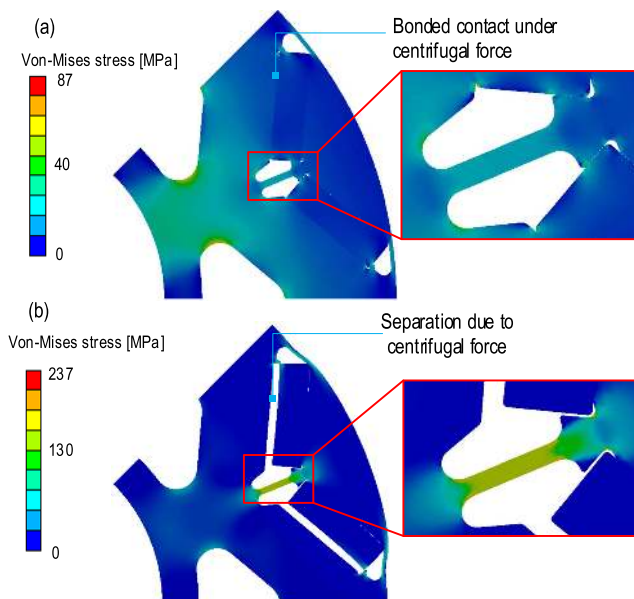Fig. 17. Contacts between parts and boundary condition in the spin analysis.

Fig. 18. Stress comparison for spin analysis with different contacts. (a) Bonded contact between magnets and rotor. (b) Frictional contact between magnets and rotor.

with symmetry boundary conditions (see Fig.17) and with fine meshing is generally used for the spin analysis [103]–[105].

In order to show how improper contacts affect the maximum stress of the rotor, Fig. 18 compares the stress distribution of a spinning rotor when the contacts between the rotor and the magnets are modeled as bonded and frictional contacts. The stress shown in Fig. 18(a), where the magnets and the rotor are modeled with a bonded contact, is much smaller than the stress shown in Fig. 18(b), where the contact between the magnets and the rotor is a frictional contact. Therefore, if bonded contact is used between the rotor and the magnets, the maximum mechanical stress of the rotor may be underestimated, and the rotor might fail in the actual operation.

After running 3-D FEA simulations for the spin analysis, motor designers can evaluate the strength of the rotor structure by comparing the maximum von Mises stress of the rotor structure and the yield strength of the rotor material. The maximum von Mises stress, σ_m, should be less than the yield strength of the material, σ_y, divided by the factor of safety

(FOS > 1). It might be hard to determine FOS for different applications. In that case, the spin analysis can be conducted 10%–20% higher than the maximum motor operating speed and at the highest operating temperature. The mechanical integrity of the rotor can be confirmed if the maximum von Mises stress in this condition is smaller than the yield strength of the rotor lamination material.

B. Rotor Dynamic Analysis

Rotor dynamics studies the lateral and torsional vibrations of all rotating components, such as the rotor with the shaft, bearings, and seals [103]. The most important parameters for the calculation of rotor dynamics are material properties of different components and the contact between them. Besides, the stiffness of the bearings needs to be calculated properly which is related to many parameters such as the bearing type, lubrication condition, operation speed, and mounting of the bearing into the housing [106].

Rotor dynamics analysis is directed toward the determination of the critical speed which corresponds to the resonance frequency of the rotor structure. At such speed, the excitation frequency becomes equal to the natural vibrational frequency of the rotor. The rotor is designed so that the operational speeds are below or in between critical speeds [107].

Due to the complexity of rotor structures in electric motors and the need for high accuracy, FEA software is usually employed for the determination of eigenfrequencies (torsional vibrational modes) and their change with rotational speed. It is worth mentioning that the change in eigenfrequencies with rotational speed is due to their dependence to gyroscopic matrix speed in the motion equation of rotor dynamics [108]. To visualize this change and the position of the critical speeds at different eigenfrequencies, Campbell diagram is widely used [109], [110].

C. Static Stress Analysis

The shaft of an electric motor is exposed to high static stress due to the torsion, bending, and axial loading. The static stress analysis is performed on the shaft to assess whether the static stress in the stress–concentration areas (e.g., keyways, notches, holes, shoulder fillets, and splines) is below the maximum allowed the stress of the materials [111].

Static stress analysis is usually conducted using FEA software packages. In [103], an example of the static stress analysis for a traction motor shaft was presented where the shaft was connected to the rotor through keyways and to the load through gears. The tangential loads on the keyway have been modeled from the torque. The tangential, radial, and axial gear loads were applied on the gear teeth model.

D. Fatigue Analysis

Even if the shaft and its key components are safe under the static load, the failure might still occur due to the repeating or fluctuating nature of the applied stress [112]. This is called fatigue failure and it appears after a certain number of stress cycles. Fatigue of the structure defines the service life of a component and it depends on material properties, manufacturing process, operating environment, and the design.

Several methods have been developed to estimate the life of the system under different loading conditions of the motor: 1) the stress-life (SN); 2) the strain-life (EN); and 3) the linear-elastic fracture mechanics (LEFM). In all of these methods, the life in number of cycles to failure is predicted for the specific level of loading. According to the value of N, fatigue life can be low-cycle failure ($1 < N < 10^3$) or high-cycle failure ($N > 10^3$) [113], [114].

A case study to model the fatigue life of a traction motor rotor has been presented in [103] using the SN method for the complete reversed loading. There are also many specialized FEA packages available for fatigue analysis [114]–[116].

VIII. CONCLUSION

This paper presents the important aspects of modeling and analysis techniques in different engineering domains for electric motors. This paper is structured to guide the electric motor designers to conduct multidisciplinary analysis, which is crucial to satisfy the performance, efficiency, reliability, and cost requirements in electric motors. The methods and techniques for dynamic modeling, loss calculations, demagnetization analysis, thermal modeling, acoustic noise and vibration analysis, and mechanical stress modeling in electric motors have been presented with examples and illustrations.

Commercial software tools can link some of these modeling techniques and provide a comprehensive multiphysics analysis workflow. This enables simulating the different design alternatives and investigates tradeoffs in each multidisciplinary domain. The techniques presented in this paper can also be used to develop analytically enhanced multidisciplinary analysis tools for various electric motors, including vehicular power and propulsion systems. The analytical models can be combined with FEA models to improve the modeling accuracy and reduce the simulation time. This enables the design and analysis of electric motor in multiple engineering disciplines to satisfy the stringent operational requirements.

ACKNOWLEDGMENT

REFERENCES

[1] J. de Santiago *et al.*, "Electrical motor drivelines in commercial all-electric vehicles: A review," *IEEE Trans. Veh. Technol.*, vol. 61, no. 2, pp. 475–484, Feb. 2012.

[2] M. Popescu, I. Foley, D. A. Stator, and J. E. Goss, "Multi-physics analysis of a high torque density motor for electric racing cars," in *Proc. IEEE Energy Convers. Congr. Expo. (ECCE)*, Montreal, QC, Canada, Sep. 2015, pp. 6537–6544.

[3] F. Momen, K. Rahman, and Y. Son, "Electrical propulsion system design of Chevrolet Bolt battery electric vehicle," *IEEE Trans. Ind. Appl.*, vol. 55, no. 1, pp. 376–384, Jan./Feb. 2019.

[4] A. Iwai, S. Honjo, H. Suzumori, and T. Okazawa, "Development of traction motor for new zero—Emission vehicle," in *Proc. IEEE Int. Power Electron. Conf.*, Niigata, Japan, May 2018, pp. 2066–2072.

[5] K. Namiki, K. Murota, and M. Shoji, "High performance motor and inverter system for a newly developed electric vehicle," SAE Tech. Paper 2018-0461, 2018. doi: 10.4271/2018-01-0461.

[6] N. R. Patel, V. A. Shah, and M. M. Lokhande, "A novel approach to the design and development of 12/15 radial field C-core switched reluctance motor for implementation in electric vehicle application," *IEEE Trans. Veh. Technol.*, vol. 67, no. 9, pp. 8031–8040, Sep. 2018.

[7] S. Okamoto, N. Denis, Y. Kato, M. Ieki, and K. Fujisaki, "Core loss reduction of an interior permanent-magnet synchronous motor using amorphous stator core," *IEEE Trans. Ind. Appl.*, vol. 52, no. 3, pp. 2261–2268, May/Jun. 2016.

[8] J. Wang, X. Yuan, and K. Atallah, "Design optimization of a surface-mounted permanent-magnet motor with concentrated windings for electric vehicle applications," *IEEE Trans. Veh. Technol.*, vol. 62, no. 3, pp. 1053–1064, Mar. 2013.

[9] Z. Makni, M. Besbes, and C. Marchand, "Multiphysics design methodology of permanent-magnet synchronous motors," *IEEE Trans. Veh. Technol.*, vol. 56, no. 4, pp. 1524–1530, Jul. 2007.

[10] A. Nasiri, "Full digital current control of permanent magnet synchronous motors for vehicular applications," *IEEE Trans. Veh. Technol.*, vol. 56, no. 4, pp. 1531–1557, Jul. 2007.

[11] S. L. Ho, W. N. Fu, and H. L. Li, "The state of art on dynamic mathematical models of induction machines: Circuit-field coupled models," in *Proc. IEEE Int. Conf. Power Electron. Drive Syst. (PEDS)*, vol. 1, Hong Kong, Jul. 1999, pp. 525–530.

[12] F. Soares and P. J. C. Branco, "Simulation of a 6/4 switched reluctance motor based on Matlab/Simulink environment," *IEEE Trans. Aerosp. Electron. Syst.*, vol. 37, no. 3, pp. 989–1009, Jul. 2001.

[13] M. Boesing, "Acoustic modeling of electrical drives," Ph.D. Dissertation, RWTH Aachen Univ., Aachen, Germany, 2014.

[14] H. Gao, F. R. Salmasi, and M. Ehsani, "Inductance model-based sensorless control of the switched reluctance motor drive at low speed," *IEEE Trans. Power Electron.*, vol. 19, no. 6, pp. 1568–1573, Nov. 2004.

[15] D. S. Mihic, M. V. Terzic, and S. N. Vukosavic, "A new nonlinear analytical model of the SRM with included multiphase coupling," *IEEE Trans. Energy Convers.*, vol. 32, no. 4, pp. 1322–1334, Dec. 2017.

[16] W. Peng and J. Gyselinck, "Magnetic-equivalent-circuit modelling of switched reluctance machines with mutual coupling effects," in *Proc. IEEE Int. Conf. Elect. Mach. (ICEM)*, Lausanne, Switzerland, Sep. 2016, pp. 426–432.

[17] B. Fahimi, G. Suresh, J. Mahdavi, and M. Ehsami, "A new approach to model switched reluctance motor drive application to dynamic performance prediction, control and design," in *Proc. Annu. IEEE Power Electron. Spec. Conf. (PESC)*, vol. 2, Fukuoka, Japan, May 1998, pp. 2097–2102.

[18] N. Bianchi and L. Alberti, "MMF harmonics effect on the embedded FE analytical computation of PM motors," *IEEE Trans. Ind. Appl.*, vol. 46, no. 2, pp. 812–820, Mar./Apr. 2010.

[19] T. J. E. Miller, M. Popescu, C. Cossar, and M. I. McGilp, "Computation of the voltage-driven flux-MMF diagram for saturated PM brushless motors," in *Proc. IEEE Ind. Appl. Conf. Annu. Meeting*, vol. 2, Hong Kong, China, Oct. 2005, pp. 1023–1028.

[20] J. Dong *et al.*, "Advanced dynamic modeling of three-phase mutually coupled switched reluctance machine," *IEEE Trans. Energy Convers.*, vol. 33, no. 1, pp. 146–154, Mar. 2018.

[21] T. Herold, D. Franck, E. Lange, and K. Hameyer, "Extension of a d-q model of a permanent magnet excited synchronous machine by including saturation, cross-coupling and slotting effects," in *Proc. IEEE Int. Electric Mach. Drives Conf. (IEMDC)*, Niagara Falls, ON, Canada, May 2011, pp. 1363–1367.

[22] G. Dajaku, "Electromagnetic and thermal modeling of highly utilized PM machines," Ph.D. dissertation, Dept. Elect. Eng. Inf. Technol., Bundeswehr Univ. Munich, Neubiberg, Germany, 2006.

[23] A. Veltman, "The fish method: Interaction between AC-machines and switching power converters," Ph.D. dissertation, Dept. Elect. Eng., Delft Univ. Technol., Delft, The Netherlands, 1994.

[24] O. V. Thorsen and M. Dalva, "Model for simulation of induction motors with parameter determination and examples of application," in *Proc. IEEE Int. Electric Mach. Drives Conf. Rec.*, Milwaukee, WI, USA, May 1997, pp. MB1/3.1–MB1/3.3.

[25] A. Campeanu, M. Radulescu, I. Vlad, and S. Enache, "Influence of cross-saturation for modeling and simulation of the dynamic processes in the induction motor," in *Proc. Int. Conf. Comput. Tool*, Warsaw, Poland, Sep. 2007, pp. 1830–1833.

[26] M. Amrhein and P. T. Krein, "Induction machine modeling approach based on 3-D magnetic equivalent circuit framework," *IEEE Trans. Energy Convers.*, vol. 25, no. 2, pp. 339–347, Jun. 2010.

[27] T. H. Akinaga, T. Staudt, W. Hoffmann, C. E. Soares, A. A. de Espíndola, and J. P. A. Bastos, "A comparative investigation of iron loss models for electrical machine design using FEA and experimental validation," in *Proc. IEEE Internal Conf. Electr. Mach. (ICEM)*, Alexandroupoli, Greece, Sep. 2018, pp. 461–466.

[28] A. Krings and J. Soulard, "Overview and comparison of iron loss models for electrical machines," *J. Elect. Eng.*, vol. 10, no. 3, pp. 162–169, 2010.

[29] D. Lin, P. Zhou, W. N. Fu, Z. Badics, and Z. J. Cendes, "A dynamic core loss model for soft ferromagnetic and power ferrite materials in transient finite element analysis," *IEEE Trans. Magn.*, vol. 40, no. 2, pp. 1318–1321, Mar. 2004.

[30] G. Bertotti, "General properties of power losses in soft ferromagnetic materials," *IEEE Trans. Magn.*, vol. 24, no. 1, pp. 621–630, Jan. 1988.

[31] F. Fiorillo and A. Novikov, "An improved approach to power losses in magnetic laminations under nonsinusoidal induction waveform," *IEEE Trans. Magn.*, vol. 26, no. 5, pp. 2904–2910, Sep. 1990.

[32] K. Yamazaki and N. Fukushima, "Iron-loss modeling for rotating machines: Comparison between Bertotti's three-term expression and 3-D eddy-current analysis," *IEEE Trans. Magn.*, vol. 46, no. 8, pp. 3121–3124, Aug. 2010.

[33] L. Chen, H. Chen, and W. Yan, "A fast iron loss calculation model for switched reluctance motors," *IET Electr. Power Appl.*, vol. 11, no. 3, pp. 478–486, Mar. 2017.

[34] A. Boglietti, R. Bojoi, A. Cavagnino, and M. Lazzari, "Core loss estimation method for PWM inverter fed induction motors," in *Proc. Annu. Conf. IEEE Ind. Electron. Soc. (IECON)*, Glendale, AZ, USA, Nov. 2010, pp. 811–816.

[35] S. Xue *et al.*, "Iron loss model for electrical machine fed by low switching frequency inverter," *IEEE Trans. Magn.*, vol. 53, no. 11, Nov. 2017, Art. no. 2801004.

[36] I. D. Mayergoyz, *Mathematical Models of Hysteresis and their Applications*, 2nd ed. New York, NY, USA: Academic, 2003.

[37] F. Ossart, E. Hug, O. Hubert, C. Buvat, and R. Billardon, "Effect of punching on electrical steels: Experimental and numerical coupled analysis," *IEEE Trans. Magn.*, vol. 36, no. 5, pp. 3137–3140, Sep. 2000.

[38] T. P. Holopainen, P. Rasilo, and A. Arkkio, "Identification of magnetic properties for cutting edge of electrical steel sheets," *IEEE Trans. Ind. Appl.*, vol. 53, no. 2, pp. 1049–1053, Mar./Apr. 2017.

[39] M. Bali, H. De Gersem, and A. Muetze, "Determination of original nondegraded and fully degraded magnetic properties of material subjected to mechanical cutting," *IEEE Trans. Ind. Appl.*, vol. 52, no. 3, pp. 2297–2305, May/Jun. 2016.

[40] L. Vandenbossche, S. Jacobs, F. Henrotte, and K. Hameyer, "Impact of cut edges on magnetization curves and iron losses in e-machines for automotive traction," in *Proc. World Electr. Veh. Symp. Exhib.*, Schenzhen, China, Sep. 2010, vol. 4, no. 3, pp. 587–596.

[41] H. Sano, K. Narita, E. Zeze, T. Yamada, U. Kazuki, and K. Akatsu, "A practical approach for electromagnetic analysis with the effect of the residual strain due to manufacturing processes," in *Proc. IEEE Energy Convers. Congr. Expo. (ECCE)*, Sep. 2016, pp. 1–7.

[42] R. Sundaria, D. G. Nair, A. Lehikoinen, A. Arkkio, and A. Belahcen, "Loss model for the effects of steel cutting in electrical machines," in *Proc. IEEE Int. Conf. Electric Machines (ICEM)*, Alexandroupoli, Greece, Sep. 2018, pp. 1260–1266.

[43] S. Iwasaki, R. P. Deodhar, Y. Liu, A. Pride, Z. Q. Zhu, and J. J. Bremner, "Influence of PWM on the proximity loss in permanent-magnet brushless AC machines," *IEEE Trans. Ind. Appl.*, vol. 45, no. 4, pp. 1359–1367, Jul. 2009.

[44] M. van der Geest, H. Polinder, and J. A. Ferreira, "Influence of PWM switching frequency on the losses in PM machines," in *Proc. IEEE Int. Conf. Electr. Mach. (ICEM)*, Berlin, Germany, Sep. 2014, pp. 1243–1247.

[45] J. Pyrhonen, T. Jokinen, and V. Hrabovcova, *Design of Rotating Electrical Machines*. Hoboken, NJ, USA: Wiley, 2008.

[46] T. A. Lipo, *Introduction to AC Machine Design* (Wisconsin Power Electronics Research Center), 3rd ed. Madison, Wisconsin: Univ. Wisconsin, 2007.

[47] R. L. Stoll, *The Analysis of Eddy Currents*. Oxford, U.K.: Clarendon, 1974.

[48] K. G. Upadhyay, *Design of Electrical Machines* (Berechnung Elektrischer Maschinen). Hoboken, NJ, USA: Wiley, 1996.

[49] D. Bauer, P. Mamuschkin, H.-C. Reuss, and E. Nolle, "Influence of parallel wire placement on the AC copper losses in electrical machines," in *Proc. IEEE Int. Electric Mach. Drives Conf. (IEMDC)*, Coeur d'Alene, ID, USA, May 2015, pp. 1247–1253.

[50] P. B. Reddy, T. M. Jahns, and T. P. Bohn, "Modeling and analysis of proximity losses in high-speed surface permanent magnet machines with concentrated windings," in *Proc. IEEE Energy Convers. Congr. Expo.*, Atlanta, GA, USA, Sep. 2010, pp. 996–1003.

[51] F. Jiancheng, L. Xiquan, B. Han, and K. Wang, "Analysis of circulating current loss for high-speed permanent magnet motor," *IEEE Trans. Magn.*, vol. 51, no. 1, Jan. 2015, Art. no. 8200113.

[52] R. Wrobel, D. E. Salt, A. Griffo, N. Simpson, and P. H. Mellor, "Derivation and scaling of AC copper loss in thermal modeling of electrical machines," *IEEE Trans. Ind. Electron.*, vol. 61, no. 8, pp. 4412–4420, Aug. 2014.

[53] C. R. Sullivan, "Computationally efficient winding loss calculation with multiple windings, arbitrary waveforms, and two-dimensional or three-dimensional field geometry," *IEEE Trans. Power Electron.*, vol. 16, no. 1, pp. 142–150, Jan. 2001.

[54] C. Roth, F. Birnkammer, and D. Gerling, "Analytical model for AC loss calculation applied to parallel conductors in electrical machines," in *Proc. IEEE Int. Conf. Electr. Mach. (ICEM)*, Alexandroupoli, Greece, Sep. 2018, pp. 1088–1094.

[55] J. Gyselinck, R. V. Sabariego, and P. Dular, "Time-domain homogenization of windings in 2-D finite element models," *IEEE Trans. Magn.*, vol. 43, no. 4, pp. 1297–1300, Apr. 2007.

[56] A. Lehikoinen, J. Ikäheimo, A. Arkkio, and A. Belahcen, "Domain decomposition approach for efficient time-domain finite-element computation of winding losses in electrical machines," *IEEE Trans. Magn.*, vol. 53, no. 5, May 2017, Art. no. 7400609.

[57] S. G. Lee, K.-S. Kim, J. Lee, and W. H. Kim, "A novel methodology for the demagnetization analysis of surface permanent magnet synchronous motors," *IEEE Trans. Magn.*, vol. 52, no. 3, Mar. 2016, Art. no. 7003404.

[58] B. Bilgin and A. Sathyan, *Fundamentals of Electric Machines* (Advanced Electric Drive Vehicles). Boca Raton, FL, USA: CRC Press, 2014.

[59] Hitachi Metals, *High-Performance Ferrite Magnet NMF Series*. [Online]. Available: http://www.hitachi-metals.co.jp/

[60] Y. Yang *et al.*, "Design and comparison of interior permanent magnet motor topologies for traction applications," *IEEE Trans. Transport. Electrific.*, vol. 3, no. 1, pp. 86–97, Mar. 2017.

[61] JMAG Co. *Thermal Demagnetization Analysis of an SPM Motor*. Accessed: Aug. 8, 2019. [Online]. Available: http://www.jmag-international.com

[62] F. P. Incropera, D. P. DeWitt, T. L. Bergman, and A. S. Lavine, *Fundamentals of Heat and Mass Transfer*. New York, NY, USA: Wiley, 2002.

[63] Y. Yang *et al.*, "Thermal management of electric machines," *IET Elect. Syst. Transp.*, vol. 7, no. 2, pp. 104–116, Jun. 2017.

[64] U. SanAndres, G. Almandoz, J. Poza, and G. Ugalde, "Design of cooling systems using computational fluid dynamics and analytical thermal models," *IEEE Trans. Ind. Electron.*, vol. 61, no. 8, pp. 4383–4391, Aug. 2014.

[65] C. Jungreuthmayer *et al.*, "A detailed heat and fluid flow analysis of an internal permanent magnet synchronous machine by means of computational fluid dynamics," *IEEE Trans. Ind. Electron.*, vol. 56, no. 12, pp. 4568–4578, Dec. 2012.

[66] P. Lindh *et al.*, "Direct liquid cooling method verified with an axial-flux permanent-magnet traction machine prototype," *IEEE Trans. Ind. Electron.*, vol. 64, no. 8, pp. 6086–6095, Aug. 2017.

[67] S. Nategh, O. Wallmark, M. Leksell, and S. Zhao, "Thermal analysis of a PMaSRM using partial FEA and lumped parameter modeling," *IEEE Trans. Energy Convers.*, vol. 27, no. 2, pp. 477–488, Jun. 2012.

[68] P. Ponomarev, M. Polikarpova, and J. Pyrhönen, "Thermal modeling of directly-oil-cooled permanent magnet synchronous machine," in *Proc. IEEE Int. Conf. Electr. Mach.*, Marseille, France, Sep. 2012, pp. 1882–1887.

[69] M. Polikarpova, P. Ponomarev, P. Lindh, I. Petrov, W. Jara, V. Naumanen, J. A. Tapia, and J. Pyrhönen, "Hybrid cooling method of axial-flux permanent-magnet machines for vehicle applications," *IEEE Trans. Ind. Electron.*, vol. 62, no. 12, pp. 7382–7390, Dec. 2015.

[70] B. Andersson, "Lumped parameter thermal modelling of electric machines analysis of an interior permanent magnet synchronous machine for vehicle applications," M.S. thesis, Dept. Energy Environ., Chalmers Univ. Technol., Gothenburg, Sweden, 2013.

[71] A. Boglietti, A. Cavagnino, and D. Staton, "Determination of critical parameters in electrical machine thermal models," *IEEE Trans. Ind. Appl.*, vol. 44, no. 4, pp. 1150–1159, Jul. 2008.

[72] A. Boglietti, A. Cavagnino, D. Staton, M. Shanel, M. Mueller, and C. Mejuto, "Evolution and modern approaches for thermal analysis of electrical machines," *IEEE Trans. Ind. Electron.*, vol. 56, no. 3, pp. 871–882, Mar. 2009.

[73] F. Qi, M. Schenk, and R. W. De Doncker, "Discussing details of lumped parameter thermal modeling in electrical machines," in *Proc. IET Int. Conf. Power Electron. (PEMD)*, Manchester, U.K., Apr. 2014, pp. 1–6.

[74] A. Boglietti, A. Cavagnino, M. Lazzari, and M. Pastorelli, "A simplified thermal model for variable-speed self-cooled industrial induction motor," *IEEE Trans. Ind. Appl.*, vol. 39, no. 4, pp. 945–952, Jul. 2003.

[75] J. Lindstrom, "Thermal model of a permanent-magnet motor for a hybrid electric vehicle," Ph.D. dissertation, Dept. Elect. Eng., Chalmers Univ. Technol., Gothenburg, Sweden, 1999.

[76] K. R. Anderson, J. Lin, C. McNamara, and V. Magri, "CFD study of forced air cooling and windage losses in a high speed electric motor," *J. Electron. Cooling Therm. Control*, vol. 5, no. 2, p. 27, Jun. 2015.

[77] D. A. Howey, P. R. N. Childs, and A. S. Holmes, "Air-gap convection in rotating electrical machines," *IEEE Trans. Ind. Electron.*, vol. 59, no. 3, pp. 1367–1375, Mar. 2012.

[78] M. Fénot, Y. Bertin, E. Dorignac, and G. Lalizel, "A review of heat transfer between concentric rotating cylinders with or without axial flow," *Int. J. Therm. Sci.*, vol. 50, no. 7, pp. 1138–1155, Jul. 2011.

[79] P. R. N. Childs, A. B. Turner, C. M. Vaughan, D. Rayner, and F. J. Bayley, "Heat transfer to a rotating drum in an annulus with a stator blade row and axial throughflow," in *Proc. ASME Int. Gas Turbine Aeroengine Congr. Expo.*, Cologne, Germany, Jun. 1992, pp. 1–4.

[80] X. Luo, X. Zhao, L. Wang, H. Wu, and G. Xu, "Flow structure and heat transfer characteristics in rotor–stator cavity with inlet at low radius," *Appl. Therm. Eng.*, vol. 70, no. 1, pp. 291–306, Sep. 2014.

[81] N. Lancial, F. Torriano, F. Beaubert, S. Harmand, and G. Rolland, "Taylor-Couette-Poiseuille flow and heat transfer in an annular channel with a slotted rotor," *Int. J. Therm. Sci.*, vol. 112, pp. 92–103, Feb. 2017.

[82] *Heat and Mass Transfer Data Book*, General Electric Co., Schenectady, NY, USA, 1977.

[83] M. L. Hosain and R. B. Fdhila, "Air-gap heat transfer in rotating electrical machines: A parametric study," *Energy Procedia*, vol. 142, pp. 4176–4181, Dec. 2017.

[84] M. L. Hosain, R. Bel Fdhila, and K. Rönnberg, "Taylor-Couette flow and transient heat transfer inside the annulus air-gap of rotating electrical machines," *Appl. Energy*, vol. 207, pp. 624–633, Dec. 2017.

[85] A. Boglietti, A. Cavagnino, D. A. Staton, and M. Popescu, "Impact of different end region cooling arrangements on endwinding heat transfer coefficients in electric motors," in *Proc. IEEE Annu. Conf. Ind. Electron.*, Porto, Portugal, Nov. 2009, pp. 1168–1173.

[86] J. Kaye and K. M. Becker, "Measurements of diabatic flow in an annulus with an inner rotating cylinder," *J. Heat Transf.*, vol. 84, no. 2, pp. 97–104, May 1958.

[87] J. E. Cousineau, K. Bennion, D. DeVoto, and S. Narumanchi, "Experimental characterization and modeling of thermal resistance of electric machine lamination stacks," *Int. J. Heat Mass Transf.*, vol. 129, pp. 152–159, Feb. 2019.

[88] J. E. Cousineau, K. Bennion, V. Chieduko, R. Lall, and A. Gilbert, "Experimental characterization and modeling of thermal contact resistance of electric machine stator-to-cooling jacket interface under interference fit loading," *ASME J. Therm. Sci. Eng. Appl.*, vol. 10, no. 4, May 2018, Art. no. 041016.

[89] A. Boglietti, E. Carpaneto, M. Cossale, S. Vaschetto, M. Popescu, and D. Stator, "Stator winding thermal conductivity evaluation: An industrial production assessment," in *Proc. IEEE Energy Convers. Congr. Expo. (ECCE)*, Montreal, QC, Canada, Sep. 2015, pp. 4865–4871.

[90] A. Boglietti, A. Cavagnino, M. Parvis, and A. Vallan, "Evaluation of radiation thermal resistances in industrial motors," *IEEE Trans. Ind. Appl.*, vol. 42, no. 3, pp. 688–693, May 2006.

[91] J. W. Jiang, J. Liang, J. Dong, B. Howey, and A. D. Callegaro, "Noise and vibration in switched reluctance machines," in *Switched Reluctance Motor Drives*. Boca Raton, FL, USA: CRC Press, 2018.

[92] H. Xing, *Advances in Geocomputing*. Berlin, Genmany: Springer, 2009.

[93] J. O. Fiedler, K. A. Kasper, and R. W. De Doncker, "Calculation of the acoustic noise spectrum of SRM using modal superposition," *IEEE Trans. Ind. Electron.*, vol. 57, no. 9, pp. 2939–2945, Sep. 2010.

[94] F. Lin, S. Zuo, W. Deng, and S. Wu, "Modeling and analysis of acoustic noise in external rotor in-wheel motor considering Doppler effect," *IEEE Trans. Ind. Electron.*, vol. 65, no. 6, pp. 4524–4533, Jun. 2018.

[95] S. Zuo, F. Lin, and X. Wu, "Noise analysis, calculation, and reduction of external rotor permanent-magnet synchronous motor," *IEEE Trans. Ind. Elect.*, vol. 62, no. 10, pp. 6204–6212, Oct. 2015.

[96] W. Cai, P. Pillay, and Z. Tang, "Impact of stator windings and end-bells on resonant frequencies and mode shapes of switched reluctance motors," *IEEE Trans. Ind. Appl.*, vol. 38, no. 4, pp. 1027–1036, Jul. 2002.

[97] A. H. Isfahani and B. Fahimi, "Comparison of mechanical vibration between a double-stator switched reluctance machine and a conventional switched reluctance machine," *IEEE Trans. Magn.*, vol. 50, no. 2, pp. 293–296, Feb. 2014.

[98] P. Pellerey, V. Lanfranchi, and G. Friedrich, "Coupled numerical simulation between electromagnetic and structural models. Influence of the supply harmonics for synchronous machine vibrations," *IEEE Trans. Magn.*, vol. 48, no. 2, pp. 983–986, Feb. 2012.

[99] J. F. Gieras, C. Wang, and J. C. Lai. *Noise of Polyphase Electric Motors*. Boca Raton, FL, USA: CRC Press, 2005.

[100] J. Dong et al., "Hybrid acoustic noise analysis approach of conventional and mutually coupled switched reluctance motors," *IEEE Trans. Energy Convers.*, vol. 32, no. 3, pp. 1042–1051, Sep. 2017.

[101] X. Guo, R. Zhong, M. Zhang, D. Ding, and W. Sun, "Fast computation of radial vibration in switched reluctance motors," *IEEE Trans. Ind. Electron.*, vol. 65, no. 6, pp. 4588–4598, Jun. 2018.

[102] F. L. M. dos Santos, J. Anthonis, F. Naclerio, J. J. C. Gyselinck, H. Van der Auweraer, and L. C. S. Goes, "Multiphysics NVH modeling: Simulation of a switched reluctance motor for an electric vehicle," *IEEE Trans. Ind. Electron.*, vol. 61, no. 1, pp. 469–476, Jan. 2014.

[103] S. Ramarathnam, A. K. Mohammed, B. Bilgin, A. Sathyan, H. Dadkhah, and A. Emadi, "A review of structural and thermal analysis of traction motors," *IEEE Trans. Transport. Electrific.*, vol. 1, no. 3, pp. 255–265, Oct. 2015.

[104] J.-W. Jung et al., "Mechanical stress reduction of rotor core of interior permanent magnet synchronous motor," *IEEE Trans. Magn.*, vol. 48, no. 2, pp. 911–914, Feb. 2012.

[105] F. Chai, Y. Li, P. Liang, and Y. Pei, "Calculation of the maximum mechanical stress on the rotor of interior permanent-magnet synchronous motors," *IEEE Trans. Ind. Electron.*, vol. 63, no. 6, pp. 3420–3432, Jun. 2016.

[106] W. Tong, *Mechanical Design of Electric Motors*. Boca Raton, FL, USA: CRC Press, 2014.

[107] M. V. Terzic, D. S. Mihic, and S. N. Vukosavic, "Impact of rotor material on the optimal geometry of high-speed drag-cup induction motor," *IEEE Trans. Energy Convers.*, vol. 31, no. 2, pp. 455–465, Jun. 2016.

[108] E. Swanson, C. D. Powell, and S. Weissman, "A practical review of rotating machinery critical speeds and modes," *Sound Vibrat.*, vol. 39, no. 5, pp. 16–17, May 2005.

[109] N. Dumitru, E. Secară, and M. Mihălcică, "Study of rotor-bearing systems using Campbell diagram," in *Proc. Int. Conf. Manuf. Eng., Qual. Prod. Syst.*, Brasov, Romania, Sep. 2009, pp. 393–396.

[110] F. C. Nelson, "Rotor dynamics without equations," *Int. J. Condition Monitor. Diagnostic Eng. Manage.*, vol. 10, no. 3, pp. 2–10, Jul. 2007.

[111] D. A. Baker, "A finite element study of stresses in stepped splined shafts and partially splined shafts under being, torsion, and combined loadings," M.S. Thesis, Dept. Mech. Eng., Virginia Polytech. Inst., Blacksburg, VA, USA, May 4, 1999.

[112] R. A. Hardin and C. Beckermann, "Prediction of the fatigue life of cast steel containing shrinkage porosity," *Metall. Mater. Trans. A*, vol. 40, no. 3, pp. 581–597, Mar. 2009.

[113] R. A. Hardin and C. Beckermann, "Integrated design of steel castings: Case studies," in *Proc. 63rd SFSA Tech. Operating Conf.*, Chicago, IL, USA, Dec. 2009, pp. 1–28.

[114] A. Winkler, S. Holt, and L. Vallance, *Concerning the Synergy of Stress and Strain-Based Methods in Modern Metal Fatigue Analysis*. Accessed: Feb. 2019. [Online]. Available: http://www.academia.edu/

[115] K. E. Hansen. (2012). Safe marine operations in wind energy: Dynamic motion analysis for wind farm drilling rig transport operation. MSC Software. Accessed: Feb. 2019. [Online]. Available: http://www.simevolution.eu/

[116] M. L. Facchinetti, B. Weber, C. Doudard, and S. Calloch. (2007). *Taking into Account the Forming Process in Fatigue Design Computations*. Accessed: Feb. 2019. [Online]. Available: http://www.ncode.com/

Berker Bilgin (S'09–M'11–SM'16) received the Ph.D. degree in electrical engineering from the Illinois Institute of Technology, Chicago, IL, USA, in 2011, and the M.B.A. degree from the DeGroote School of Business, McMaster University, Hamilton, ON, Canada, in 2018.

He was the Chief Engineer and the Research Program Manager in Canada Excellence Research Chair in Hybrid Powertrain Program with the McMaster Institute for Automotive Research and Technology (MacAUTO), McMaster University. He is currently an Assistant Professor with the Department of Electrical and Computer Engineering (ECE), McMaster University. He is the Co-Founder and the Vice President of Engineering of Enedym Inc., Hamilton, ON, Canada, which is a spin-off company of McMaster University. Enedym specializes in electric machines, electric motor drives (EMDs), advanced controls and software, and virtual engineering. Dr. Bilgin has authored or coauthored 81 journals and conference papers and 3 book chapters. He is the Principal Inventor/Co-Invertor of ten patents and pending patent applications. His current research interests include electric machines, switched reluctance motor (SRM) drives, acoustic noise and vibration analysis and reduction, power electronics and EMDs. He is the lead editor and author of the textbook *SRM Drives: Fundamentals to Applications*.

Dr. Bilgin was the Elected General Chair of the 2016 IEEE Transportation Electrification Conference and Expo (ITEC). He has served as an Associate Editor for the IEEE TRANSACTIONS ON TRANSPORTATION ELECTRIFICATION.
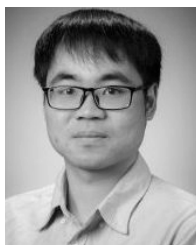
Jianbin Liang received the B.S. degree in mechanical engineering and the M.S. degree in vehicle engineering from the State Key Laboratory of Mechanical Transmissions, Chongqing University, Chongqing, China, in 2012 and 2015, respectively. He is currently pursuing the Ph.D. degree with the McMaster Automotive Resource Center (MARC), McMaster University, Hamilton, ON, Canada, as part of the Canada Excellence Research Chair in Hybrid Powertrain Program.

His current research interests include acoustic noise reduction of electric machines.

Mladen V. Terzic (S'12–M'16) received the B.Eng., M.Sc., and Ph.D. degrees from the Faculty of Electrical Engineering, University of Belgrade, Belgrade, Serbia, in 2007, 2009, and 2015, respectively.

He has been a Teaching and Research Assistant with the Department of Power Converters and Drives, Faculty of Electrical Engineering, University of Belgrade, where he became Assistant Professor in 2015. In 2016 and 2017, he was a Post-Doctoral Research Fellow on the design of electrical machines for various electric vehicles with the McMaster Institute for Automotive Research and Technology, McMaster University, Hamilton, ON, Canada. He is currently an Electrical Machines Specialist with Rheinmetall Automotive GmbH, Neuss, Germany, where he is responsible for the design, analysis and testing of electrical machines and actuators for wide range of applications in all types of vehicles. His current research interests include field of electrical machines design and power electronics, mainly for automotive applications.

Jianning Dong (S'12–M'17) received the B.S. and Ph.D. degrees in electrical engineering from Southeast University, Nanjing, China, in 2010 and 2015, respectively.

He was a Post-Doctoral Researcher with the McMaster Automotive Resource Center, McMaster University, Hamilton, ON, Canada. Since 2016, he has been an Assistant Professor with the DC System, Energy Conversion and Storage (DCE&S) Group, Delft University of Technology (TU Delft), Delft, The Netherlands. His current research interests include electromechanical energy conversion and contactless power transfer.

Romina Rodriguez (SM'15) received the B.S. and M.S. degrees in mechanical engineering from the University of California at Berkeley, Berkeley, CA, USA. She is currently pursuing the Ph.D. degree with the Mechanical Engineering Department, McMaster University, Hamilton, ON, Canada.

From 2012 to 2014, she was a Mechanical Engineer with the Thermal Design & Analysis Group, Northrop Grumman, Azusa, CA, USA. Her current research interests include thermal management of power electronics and electric machines and energy harvesting technologies.

Elizabeth Trickett received the B.Sc. in physics (Hons.) and the M.ASc. in materials science and engineering, both from McMaster University, Hamilton, ON, Canada, in 2011 and 2013, respectively, where he is currently pursuing the Ph.D. degree in mechanical engineering, under the supervision of Dr. A. Emadi.

In 2015, she was with CanmetMATERIALS, Hamilton, where she was involved in nuclear, defense, and automotive research. Her current research interests include electrical steel, graphene nanocomposites, motor thermal management and design, and radiation heat transfer.

Ali Emadi (S'98–M'00–SM'03–F'13) received the B.S. and M.S. degrees (Hons.) in electrical engineering from the Sharif University of Technology, Tehran, Iran, in 1995 and 1997, respectively, and the Ph.D. degree in electrical engineering from Texas A&M University, College Station, TX, USA, in 2000.

He was a Harris Perlstein Endowed Chair Professor of engineering and the Director of the Electric Power and Power Electronics Center and Grainger Laboratories, Illinois Institute of Technology (Illinois Tech), Chicago, IL, USA, where he established research and teaching facilities and courses in power electronics, motor drives, and vehicular power systems. He was the Founder, the Chairman, and the President of Hybrid Electric Vehicle Technologies, Inc. (HEVT)—a university spin-off company of Illinois Tech. He is currently the Canada Excellence Research Chair Laureate with McMaster University, Hamilton, ON, Canada.

Dr. Emadi was the Inaugural General Chair of the 2012 IEEE Transportation Electrification Conference and Expo (ITEC). He was the Chair of several IEEE and SAE conferences in the areas of vehicle power and propulsion. He is the NSERC/FCA Industrial Research Chair of electrified powertrains and the Tier I Canada Research Chair of transportation electrification and smart mobility. He was a recipient of numerous awards and recognitions. He was the Advisor of the Formula Hybrid Teams, Illinois Tech and McMaster University, which received the GM Best Engineered Hybrid System Award at the 2010, 2013, and 2015 competitions. He is the principal author/coauthor of more than 450 journals and conference papers and several books including *Vehicular Electric Power Systems* (2003), *Energy Efficient Electric Motors* (2004), *Uninterruptible Power Supplies and Active Filters* (2004), *Modern Electric, Hybrid Electric, and Fuel Cell Vehicles* (2nd edn., 2009), and *Integrated Power Electronic Converters and Digital Control* (2009). He is the Editor of the *Handbook of Automotive Power Electronics and Motor Drives* (2005) and *Advanced Electric Drive Vehicles* (2014). He is also the Coeditor of the *Switched Reluctance Motor Drives*(2018). He is the Founding Editor-in-Chief of the IEEE TRANSACTIONS ON TRANSPORTATION ELECTRIFICATION.